crystals

MDPI

Article

RETRACTED: The Effect of Treatment Temperature on Microstructure and Mechanical Behavior of a Fine-Grained YSZ–NiO(Ni) Anode Material

Bogdan Vasyliv [1,*], Volodymyr Kulyk [2], Zoia Duriagina [2,3] and Taras Kovbasiuk [2]

[1] Department of Hydrogen Technologies and Alternative Energy Materials, Karpenko Physico-Mechanical Institute, 5 Naukova Street, 79060 Lviv, Ukraine
[2] Department of Materials Science and Engineering, Lviv Polytechnic National University, 12 S. Bandera Street, 79013 Lviv, Ukraine; kulykvolodymyrvolodymyrovych@gmail.com (V.K.); zduriagina@ukr.net (Z.D.); felcproject@gmail.com (T.K.)
[3] Department of Materials Engineering, John Paul II Catholic University of Lublin, 14 Racławickie Aleje, 20-950 Lublin, Poland
* Correspondence: mechengin1111@gmail.com

Abstract: Reduction–oxidation (redox) cycling of a solid oxide fuel cell (SOFC) due to leakage of a fuel or standby and shutdown cycling is an issue that has attracted the attention of many research groups for a long time. The researchers mainly note the harmful effects of redox cycling on the microstructure of SOFC constituents and search for ways to mitigate or diminish them. The purpose of this study was to use reduction and oxidation stages in an appropriate mode as a positive preconditioning to improve redox cycling stability of Ni-containing SOFC anode materials. The redox treatment was applied to YSZ–NiO(Ni) anode substrate specimens at 600 °C and 800 °C. The mechanical tests (flexural strength, microhardness, and fracture toughness) were performed on these specimens and the results were compared to those for as-sintered and one-time reduced specimens. Microstructure and fracture surface morphology of material in corresponding modes were analyzed. The main findings were summarized as follows: (i) Redox treatment at 600 °C provides an increase in flexural strength and electrical conductivity of YSZ–NiO(Ni) anode cermets; (ii) the treatment at 800 °C causes formation of a gradient microstructure with lateral cracks that result in a significant decrease in flexural strength; (iii) the mode of redox treatment at 600 °C for 4 h in Ar–5% H_2/air atmosphere provides an increase in flexural strength of YSZ–NiO(Ni) anode cermets (up to 127 ± 4 MPa), while electrical conductivity was provided at a comparatively high level (7×10^5 S/m).

Keywords: solid oxide fuel cell; YSZ–NiO(Ni) anode substrate; hydrogen; microstructure; strength; microhardness; fracture toughness; fracture micromechanism

Citation: Vasyliv, B.; Kulyk, V.; Duriagina, Z.; Kovbasiuk, T. RETRACTED: The Effect of Treatment Temperature on Microstructure and Mechanical Behavior of a Fine-Grained YSZ–NiO(Ni) Anode Material. *Crystals* **2023**, *13*, 944. https://doi.org/10.3390/cryst13060944

Academic Editor: Sergio Brutti

Received: 29 May 2023
Revised: 8 June 2023
Accepted: 9 June 2023
Published: 12 June 2023
Retracted: 15 July 2024

1. Introduction

1.1. Importance of Studying Electrodes of Solid Oxide Fuel Cells

Renewable energy is a promising source for clean electricity aimed at solving climate change issues [1]. In the reviews of Golkhatmi S.Z. et al. [2], Boldrin P. et al. [3], and Jacobson A.J. [4], it was shown that among the environmentally-friendly devices serving this purpose, solid oxide fuel cells (SOFCs) have significant advantages in efficiency as they employ an electrochemical conversion method of electricity production from direct fuel oxidation. Zamudio-García J. et al. [5] showed that symmetrical SOFCs are ones of the most promising in this field. Recently, many research laboratories are working on the development and improvement of reliable materials for SOFCs as well as on the SOFC design [6–12]. Along with solid electrolyte and cathode materials [6,10,11,13–25], great attention is paid to SOFC anode materials [8,12,26–29]. It is known that fuel loss may occur during operation of a SOFC which usually leads to re-oxidation of the nickel-containing

This paper has been retracted. A retraction notice was published on 15 July 2024 in *Crystals* **2024**, *14*, 648. https://doi.org/10.3390/cryst14070648

anode [2,30–33]. Thereafter, reduction in nickel oxide should be performed to reactivate the anode material. These reduction/oxidation (redox) cycles may occur several times during SOFC operation, and thus affect its long-term stability and performance [32,34,35]. Therefore, the understanding of the effects of redox cycling on SOFC behavior, focusing on a nickel/yttria-stabilized zirconia cermet, is essential as it assists in reaching a perfect quality of developed materials for SOFC anodes.

1.2. Studying the Harmful Effects of the Cyclic Redox Process on Microstructure of SOFC Materials

Wood T. and Ivey D.G. [30] investigated the reaction kinetics and changes in mechanical properties of a SOFC under redox conditions as well as their impact on SOFC performance. Wood A. and Waldbillig D. [36] and Waldbillig D. et al. [37] found that the harmful effects of the cyclic redox process on the microstructure of SOFC materials can be mitigated or diminished using the proposed methods, in particular, the preconditioning treatment to enhance redox tolerance of SOFCs.

In the study of Li J. et al. [38], an effect of moisture on microstructure degradation and mechanical properties of the nanostructured coatings based on yttria-stabilized zirconia (n-YSZ) was studied. The authors found that hydrothermal degradation of the n-YSZ coatings resulted in pores and microcracks and caused the transformation of tetragonal to monoclinic zirconia phase, which in turn, provoked variations in the internal stress. All these microstructural changes were followed by a significant decrease in Young's modulus, flexural strength, and fracture toughness of the n-YSZ coatings.

Mack J.B. et al. [39] studied the evolution of lamellar microstructure of freeze-cast Fe-25Ni foam as material for iron–air batteries operated under conditions of cyclical steam oxidation and hydrogen reduction, and noted the eventual degradation of its internal architecture. The foam was designed as a composite with colonies of parallel lamellae separated by channels to compensate for changes in volume during the cyclical oxidation and reduction in Fe in the battery. The authors proposed a mechanism for developing an outer Fe-oxide scale over Ni during oxidation and Ni acting as a catalyst during reduction with formation of the interdiffused and homogenized Fe-rich shell and the Ni-rich core. They revealed that this cyclic process eliminates both Kirkendall pores and microchannels from the lamellae. Due to Ni alloying, Fe-25Ni foam maintains high active surface area (a channel porosity > 40%) after 10 redox cycles, in contrast to pure Fe foam showing an almost complete loss of the channel porosity.

The redox cycling behavior of lamellar Fe foams with 15 vol% fibers, created by freeze-casting, was studied by Pennell S. and Dunand D. [40]. Long zirconia fibers and long (1–2 mm) and short (0.1 mm) stainless steel fibers were used. The material was undergone to cyclic H_2/H_2O exposure at 800 °C. The authors revealed fiber engulfment as a novel degradation mechanism occurred during redox cycling in this material. As a result, foam architecture changed after the cycling from bridged-lamellar (with evenly distributed porosity) to mixed lamellar/fibrous (with unevenly distributed porosity).

Wang M. et al. [41] designed a dual-layered SOFC anode consisting of a Ni–Fe alloy layer and a Ni–YSZ cermet layer. The cell supported on this anode with straight pore paths exhibited a maximum power density of 1070 $mW \cdot cm^{-2}$ at 800 °C. The SOFC supported on the Ni-YSZ/Ni–Fe dual-layered anode did not degrade during eight redox cycles, whereas the cell supported on the Ni-YSZ single-layered anode failed after the first redox cycle. The reason for the significant improvement in the anode stability was assumed to be the straight pore paths, which allowed for fast gas phase transport. This, in turn, improved the accessibility of electrochemical reaction sites and, as a result, reduced the activation polarization.

1.3. The Ways to Improve Redox Stability of SOFC Materials

In the study of Chang H. et al. [42], a double-perovskite $Sr_2MoFeO_{6-\delta}$ (SMFO) applied over a Ni-YSZ anode to improve coking resistance in SOFCs operating on methane-based fuels was investigated. This material works as a redox-stable independent on-cell reform-

ing catalyst. It was found that the cell modified with double-layered SMFO–Al_2O_3 has improved performance when fueled with methane-based gas, as compared to a cell without the catalyst layer. In contrast, a more intense coking was revealed in the cell fueled with wet coal-bed gas (CBG), which is attributed to the presence of heavy carbon compounds in CBG. When operated on wet CH_4 at 800 °C, a Ni-YSZ anode-supported cell with SMFO generates a high power output of 1.77 $W \cdot cm^{-2}$ exhibiting improved stability.

Lv H. et al. [43] presented a low-cost and simple dip coating and one-step co-sintering technology to produce a metal supported micro-tubular SOFC with good electrochemical performance at 800 °C. They developed a SOFC sandwich structure containing Sr as "porous 430 stainless steel support | 430 stainless steel-SSZ | SSZ | porous SSZ". It was shown that the structure of the single cell did not degrade as no crack and Sr diffusion were observed after 14 thermal cycles between 600 °C and 800 °C, but the power density was lowered by 19.6%. The relatively fast degradation of microstructure was related to the agglomeration of coarsened Ni and LSM particles.

In the studies of Faes A. et al. [44], Ettler M. et al. [45], Peraldi R. et al. [46], and Mori M. et al. [47], reviews of the effects and parameters influencing redox cycles of the Ni-ceramic anode were presented. The authors described solutions for redox instability taking into account many factors, such as stack design, cell design, new materials, and microstructure optimization. They also exhibited the behavior of Ni-based anode supports with optimized microstructures under redox cycling conditions. In a series of scientific works, a controlled redox cycle was proposed to apply for the enhancement of the redox stability [36,37,44]. The reason for this was the attempt to change the material microstructure. On preconditioned specimens (one redox at 550 °C), a lower decrease in performance (3.2% decrease in voltage at 0.75 A/cm^2 after a redox cycle at 750 °C) was found compared to three times higher decrease in specimens without the treatment. Wood A. and Waldbillig D. [36] proposed the application of the initial controlled redox cycle in various stages of the anode fabrication, namely, on the powder mixture prior to the formation of the green anode, on the sintered anode before insertion in the stack, and in situ in the stack.

Pihlatie M. et al. [48] showed an increase in electrochemical performance after a redox cycle at 650 °C in a symmetrical cell configuration. Moreover, Waldbillig D. et al. [37] and Lang M. et al. [49] announced an increase in performance over short-term redox cycles. They assumed that this is due to the formation of a porous GDC barrier layer between electrolyte substrate and air electrode preventing interdiffusion at the interface.

Similarly to these last works and in contrast to other works, we showed in our previous research [27,50,51] that redox may be used as a positive phenomenon for improving long-term stability and performance of ScCeSZ–NiO(Ni) and YSZ–NiO(Ni) anode cermets. For this purpose, a corresponding redox treatment mode was set which comprised of a stage of heating the material in vacuum and intermediate degassing between the stages of reduction and oxidation. Controlled microstructure evolution during reduction and oxidation cycles allowed for the redox-stable microstructure to be obtained. As a result, a significant increase in flexural strength (by about 12–25%) and electrical conductivity (up to an acceptable level) was achieved at 600 °C.

1.4. The Use of Redox Treatment for Improvement of SOFC Performance

The analyzed above works highlight controversial hypotheses concerning redox effects on microstructure and mechanical properties of Ni-containing anode materials for SOFCs. In the case of a controlled redox mode, significant positive effects may be achieved.

The main aim of our work was to study the mechanical behavior of YSZ–NiO(Ni) anode substrate specimens that underwent the redox treatment in low-temperature (600 °C) and intermediate-temperature (800 °C) modes in comparison with the behavior of as-sintered and one-time reduced specimens. Relation of the mechanical behavior to microstructure and fracture surface morphology of material in the applied modes is to be studied, and an appropriate treatment mode for providing high redox cycling stability of Ni-containing SOFC anode materials is to be found. The main conclusions of the work

are as follows: Redox treatment at 600 °C provides an increase in flexural strength and electrical conductivity of YSZ–NiO(Ni) anode cermets, such as the treatment at 800 °C causes formation of a gradient microstructure with lateral cracks initiated on the "near-surface layer/specimen core" interfaces that results in a significant decrease in flexural strength of the material; the mode of redox treatment at 600 °C for 4 h in Ar–5% H_2/air atmosphere can be regarded as promising for preconditioning YSZ–NiO anode ceramics; residual compressive stresses that arose in redox-treated material contributed to an increase in its flexural strength compared to that of other reduced cermets (the values of flexural strength and relative strength were 127 ± 4 MPa and 96 ± 2.5%, respectively); and electrical conductivity was provided at a level of 7×10^5 S/m. These results verify the feasibility of redox technique in appropriate modes for preconditioning Ni-containing SOFC anode materials rather than using a traditional one-time reduction process.

2. Materials and Methods

The studied anode ceramics of YSZ–NiO system (yttria-stabilized zirconia–50 wt% nickel oxide) were prepared by tape casting. Initial commercial powders were as follows: YSZ (8 mol% Y_2O_3) with the average grain size of Y_2O_3 powder of 10–30 nm, of 99.95% purity and ZrO_2 powder of 30–60 nm, of 99.9% purity (IoLiTec Inc., Tuscaloosa, AL, USA); NiO of 99.5% purity with the average grain size of 40–60 nm (IoLiTec Inc., Tuscaloosa, AL, USA). Tape-casted plates were sintered at a temperature of 1400 °C for 2 h in an argon atmosphere. Specimens $1 \times 6 \times 24$ mm^3 in size were cut with a diamond disk from the 1 mm thick plates and grinded manually on their side surfaces using silicon carbide paper up to 2000 grit. The final size of the specimens was about $1 \times 5 \times 24$ mm^3. Sets of specimens were one-time reduced at 600 °C for 4 h or at 800 °C for 1 h (or 2 h) in a hydrogenous atmosphere (hydrogen of 99.99 vol.%H_2 purity or Ar–5 vol%H_2 mixture) under the pressure of 0.15 MPa (Table 1 and Figure 1a). Separate sets of specimens were undergone to the redox treatment. Five cycles of redox treatment were applied to the as-sintered ceramics (Figure 1b) in the following mode [27]: Heating in vacuum from 20 °C to 600 °C (or 800 °C); reduction in a hydrogenous atmosphere at 600 °C (or 800 °C) under the pressure of 0.15 MPa; gas evacuation; oxidation in air at 600 °C (or 800 °C); cooling down to 20 °C in air. Duration of reduction/oxidation stage was set after a thorough analysis of literature data concerning partial or complete reduction in YSZ–NiO ceramics [2,6,30,32,34,37,52]. Redox cycling of specimens was followed by their reduction in a hydrogenous atmosphere at 600 °C for 4 h or at 800 °C for 1 h under the pressure of 0.15 MPa. Finally, specimens were cooled in argon. The heating/cooling rate of 20 °C/min was set for all the modes.

Table 1. The treatment modes, electrical conductivity (σ), and flexural strength (σ_f) of tested materials.

Mode Marking	Treatment Mode (Gas Mixture Composition in vol%)	$\sigma \times 10^{-5}$ (S/m)		σ_f (MPa)	
		Mean Value	Standard Deviation	Mean Value	Standard Deviation
1	As-sintered	(*)	(*)	132.3	±4.4
2	Processing at 600 °C for 4 h in Ar–5% H_2	2.7	±0.4	111.1	±4.6
3	Processing at 600 °C for 4 h in H_2	7.9	±0.6	63.5	±6.7
4	Redox at 600 °C for 4 h in Ar–5% H_2/air	7.0	±0.4	127.0	±4.0
5	Redox at 600 °C for 4 h in H_2/air	7.3	±0.5	83.3	±4.3
6	Processing at 800 °C for 1 h in Ar–5% H_2	6.4	±0.6	54.2	±4.4
7	Processing at 800 °C for 2 h in Ar–5% H_2	5.2	±0.4	50.3	±6.3
8	Redox at 800 °C for 1 h in Ar–5% H_2/air	3.4	±0.6	43.7	±6.6

(*) Electrical conductivity is very low.

A three-point bending test of specimens was performed at 20 °C in air using a self-made loading unit installed on MTS E43.004 (MTS Systems Corporation, Eden Prairie, USA) testing machine. The cross-head speed was 10^{-3} mm/s, and the span between

the supporting roller of the unit was 14 mm. Flexural strength of material σ_f (MPa) was calculated by the equation presented by Gere J.M. and Timoshenko S.P. [53]:

$$\sigma_f = \frac{1.5 \cdot P \cdot s}{b \cdot w^2} \quad (1)$$

where P is the fracture load (N), s is the span between supporting rollers (mm), and b and w are the width and height (mm) of the test specimen, respectively.

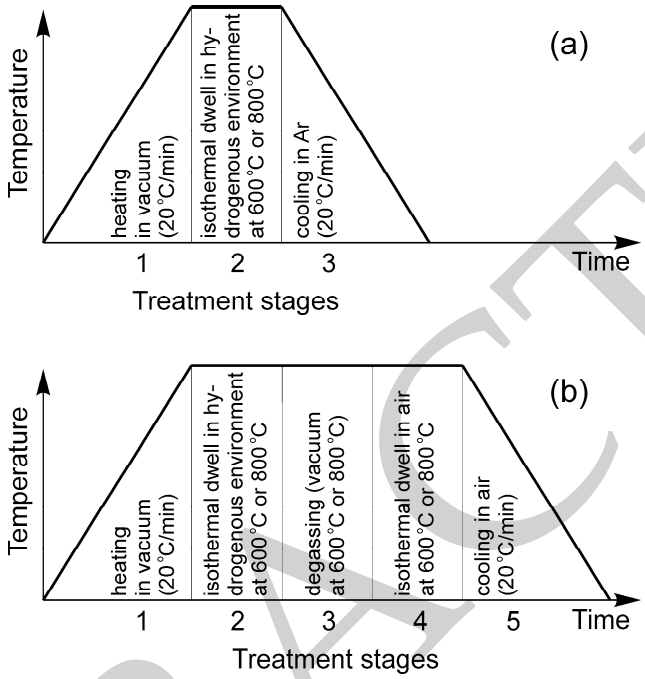

Figure 1. Schematic of (**a**) one-time processing mode and (**b**) redox treatment mode for the materials tested.

Based on results of five specimens of each material variant, the average value of flexural strength was calculated and the standard deviation was determined (Table 1). The relative strength $100 \times \sigma_f/\sigma_{f0}$ (in %) where σ_{f0} is the flexural strength of the as-sintered YSZ–NiO ceramics (mode 1) was also calculated.

A microhardness tester NOVOTEST TC-MKB1 (Novotest, Novomoskovsk, Ukraine) was used to measure Vickers microhardness of the studied materials in modes 1–8 under indentation loads of 0.49 N, 0.98 N, 1.96 N, 2.94 N, 4.91 N, and 9.81 N. We made 10 indentations for each load level and calculated Vickers microhardness (in GPa) according to the relevant standards [54,55] using the following formula:

$$H = 0.0018544\left(\frac{P}{d^2}\right) \quad (2)$$

where P is the indentation load (N), and d is the average length of the diagonals of the indentation imprint (mm).

The imprint and crack geometry was estimated with an optical microscope Neophot-21 (Zeiss, Oberkochen, Germany).

The critical stress intensity factor (SIF), K_{Ic}, is a measure of fracture toughness of material and allows for characterizing its propensity to brittle fracture due to the nucleation and propagation of cracks [13,19,21,22,24]. According to our previous works [25,27], the following formula developed by Anstis G.R. et al. [56] best fits the characterization of the YSZ-based ceramics:

$$K_{Ic} = 0.016\left(\frac{E}{H}\right)^{1/2}\left(\frac{P}{c^{3/2}}\right) \quad (3)$$

where E is Young's modulus (GPa), H is microhardness (GPa), P is the indentation load (N), and c is the radial crack length (m).

Therefore, based on the obtained values of microhardness for the studied materials in modes 1–8, we calculated the fracture toughness of the materials by this formula.

A scanning electron microscope (SEM) Carl Zeiss EVO-40XVP (Zeiss, Oberkochen, Germany) was used for analyzing material microstructure and morphology of the fracture surfaces of tested specimens. An energy-dispersive X-ray (EDX) microanalysis was performed with an INCA Energy 350 system (Oxford Instruments, Abingdon, UK).

X-ray diffraction (XRD) studies were carried out using a DRON-4.07M diffractometer (Bourevestnik, St. Petersburg, Russia) with Cu Kα radiation and Bragg–Brentano type geometry operating at 40 kV and 15 mA in 2θ angular range of 20–90°, with a step of 0.0217°. The size of a coherent dispersion area of nickel phase, D, was calculated for each material using the Win CSD software [57]. Moreover, the spacing between the planes in the atomic lattice, d, of zirconia phase (line (220)) was evaluated by the Rietveld method [57], and the residual stress, σ_r, was calculated by the following equation:

$$\sigma_r = -\frac{E(d - d_0)}{\nu \cdot d_0} \quad (4)$$

where E is Young's modulus, ν is Poisson's ratio, and d_0 is the spacing between the planes in the atomic lattice of zirconia phase ((220) line) for the as-sintered material. The values of E and ν were set according to the study of Sun B. et al. [33].

The specific electrical conductivity σ of materials (Table 1) was measured in air at 20 °C using the four-probe method according to the relevant standard [58]. For this purpose, a four-probe device ST2558B-F01A (Suzhou Jingle Electronics Technology Co., Suzhou, China) was used.

3. Results

3.1. Evolution of Microstructure at a Temperature of 600 °C

It is known that reduction in nickel oxide in YSZ–NiO ceramics should be performed to activate the anode material for SOFC operation, in particular, to achieve its appropriate electrical conductivity. For this purpose, various treatment modes were applied to the as-sintered material, resulting in quite different values of electrical conductivity (Table 1). Moreover, different flexural strengths of the treated cermets (Table 1 and Figure 2a) were caused by structural transformations that occurred in the treatment process. According to XRD analysis, as-sintered YSZ–NiO ceramics contained peaks of the YSZ and NiO phases (line 1 in Figure 3). In contrast, the materials treated according to modes 2 and 3 exhibited, in addition to the peaks of the YSZ and NiO phases, peaks of the Ni phase (lines 2 and 3 in Figure 3, respectively). The intensity of the peaks of the Ni phase increased for the material treated in mode 3 compared to that in mode 2, whereas the trend for the peaks of the NiO phase was opposite.

Partial reduction in the NiO-phase particles by diffusion mechanism [27,31,32,34–37] was achieved during exposition of as-sintered ceramics in Ar–5 vol%H_2 mixture at 600 °C for 4 h (mode 2 in Table 1). This mode can be used for gradual reduction in NiO-containing anode materials (Figure 4a). Based on EDX analysis, it was shown that 0.10–0.25 μm thick Ni-fringes were formed around NiO particles in this treatment mode (Figure 4c and Table 2). In particular, spectrum S1 showed great weight percentages of Zr and Y corresponding to the YSZ phase, spectrum S2 exhibited the presence of only Ni and O with the ratio corresponding to the NiO phase, and spectrum S3 showed the presence of all the elements (O, Ni, Y, Zr) constituting the YSZ, NiO, and Ni phases. In addition, a detailed study of a thin fringe using the line scan EDX chemical analysis (Figure 4g,h) exhibited the presence of the maximal amount of pure Ni. Electrical conductivity of about 2.7×10^5 S/m was provided by the network of thin Ni-fringes (Figure 4c).

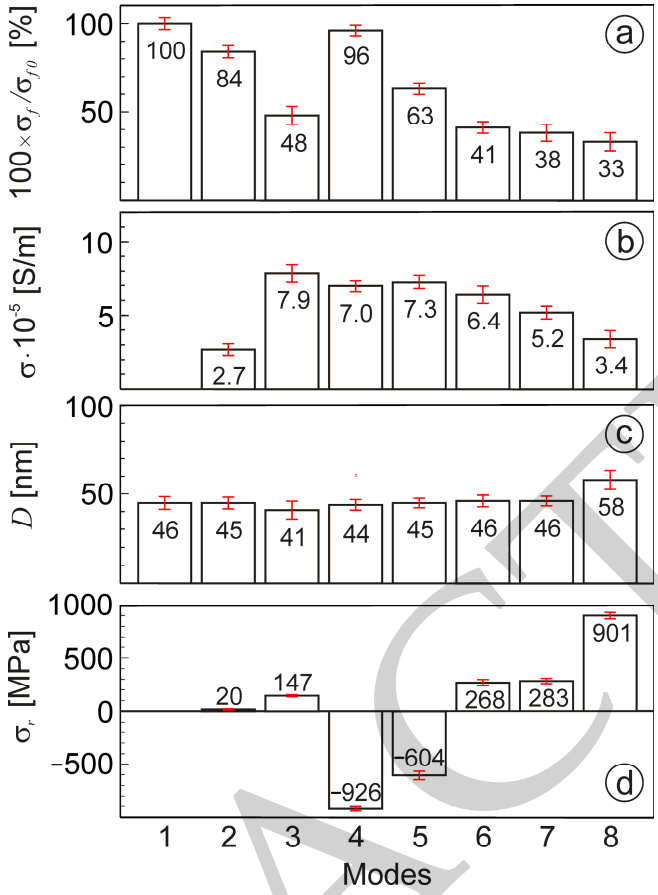

Figure 2. Relative strength $100 \times \sigma_f/\sigma_{f0}$ (**a**), specific electrical conductivity σ (**b**), size of coherent dispersion areas of nickel phase *D* (**c**), and residual stresses σ_r in the zirconia phase (**d**) for materials processed in modes 1–8 (Table 1); the numbers above or inside the bars indicate the average values of corresponding parameters; the segments in red color show the standard deviations for corresponding parameters.

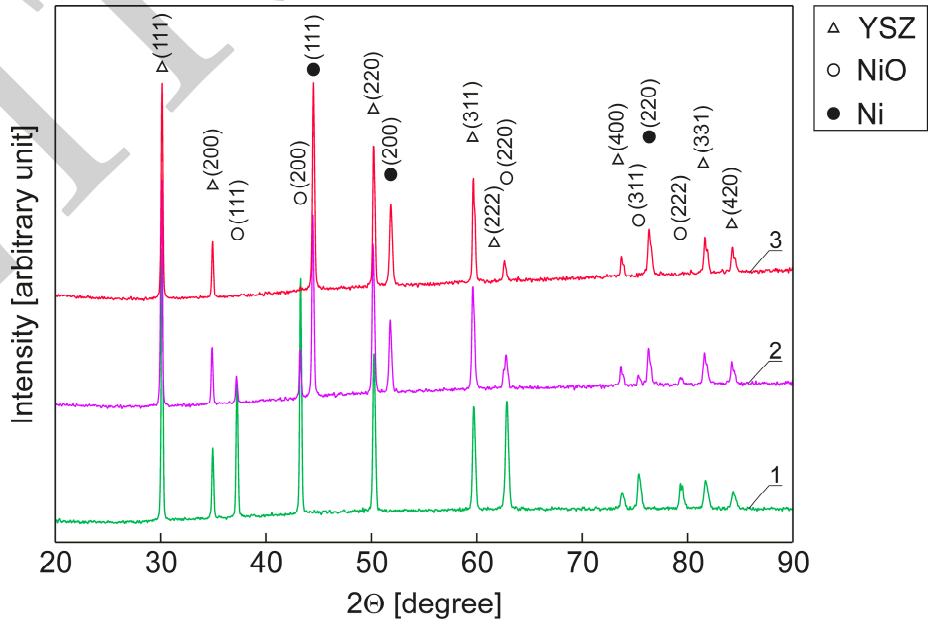

Figure 3. XRD patterns of as-sintered YSZ–NiO ceramics (of mode 1) treated according to modes 2 and 3 (Table 1) showing corresponding peaks for the YSZ, NiO, and Ni phases (see legend) and corresponding Miller indices (in parentheses).

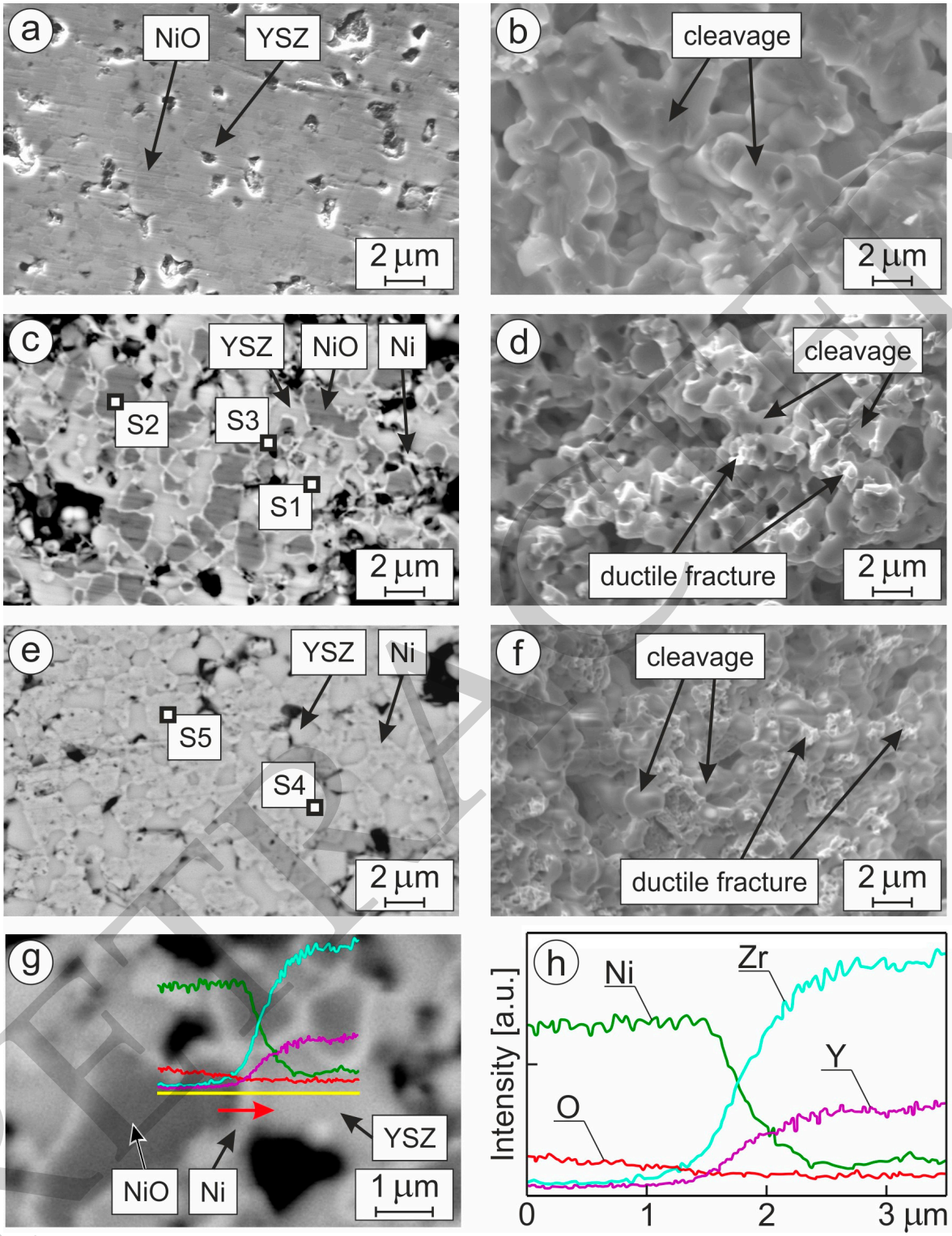

Figure 4. SEM images of (**a**,**c**,**e**,**g**) microstructure (BSD mode) and (**b**,**d**,**f**) fracture surface (SE mode) for (**a**,**b**) as-sintered YSZ–NiO ceramics (of mode 1) treated according to (**c**,**d**,**g**) mode 2 and (**e**,**f**) mode 3 (Table 1). Spectra of local EDX analyses S1, S2, and S3 are marked in SEM image (**c**) and spectra S4 and S5 are marked in SEM image (**e**). A red arrow in the magnified SEM image (**g**) indicates a direction of the line scan EDX chemical analysis resulting in (**h**) corresponding spectra of zirconium, yttrium, nickel, and oxygen. Arrows indicate the YSZ, NiO, and Ni phases, as well as cleavage and ductile fractures.

Table 2. The data of the EDX spectra S1, S2, and S3 marked in Figure 4c for a specimen treated in mode 2.

Chemical Element and X-ray Series	Spectra					
	S1		S2		S3	
	wt%	at%	wt%	at%	wt%	at%
O K	26.85	66.85	25.42	55.58	8.43	27.74
Ni K	4.65	3.15	74.58	44.42	60.72	54.41
Y L	7.50	3.36	–	–	3.39	2.01
Zr L	61.00	26.64	–	–	27.46	15.84

Due to the exposure of as-sintered ceramics in pure hydrogen at 600 °C for 4 h (mode 3 in Table 1) and more intensive diffusion [27,31,32,34–37], the microstructure was formed which comprised completely reduced Ni particles by diffusion mechanism (Figure 4e), and a simultaneous volume decrease in initial NiO particles of 41.6% occurred as described in the articles of Sarantaridis D. and Atkinson A. [32] and Sun B. et al. [33]. In particular, spectrum S4 exhibited high weight percentages of Zr and Y corresponding to the YSZ phase (Table 3) similarly to spectrum S1 in mode 2, whereas spectrum S5 exhibited the presence of only Ni and a low percentage of oxygen that corresponds to the Ni phase. Complete reduction in the nickel phase ensured high electrical conductivity of the cermet (Figure 2b).

Table 3. The data of the EDX spectra S4 and S5 marked in Figure 4e for a specimen treated in mode 3.

Chemical Element and X-ray Series	Spectra			
	S4		S5	
	wt%	at%	wt%	at%
O K	26.17	66.32	2.50	8.59
Ni K	3.18	2.19	97.50	91.41
Y L	7.65	3.49	–	–
Zr L	63.00	28.00	–	–

According to our earlier results [50,51], interdiffusion of Ni and O elements on boundaries of contacting Ni-phase particles occurs during redox treatment of a Ni-containing cermet at 600 °C, and thus causes an increase in material strength compared to that of the one-time reduced material. In the microstructure image of the redox-treated cermet at 600 °C for 4 h in Ar–5% H_2/air atmosphere (mode 4 in Table 1 and Figure 5a), we can see completely reduced small Ni-phase particles and large particles with thicker Ni-fringes (about 0.25–0.40 μm) and relatively smaller NiO core area compared to that of the cermet one-time reduced in Ar–5% H_2 atmosphere (mode 2 in Table 1 and Figure 4c). This treatment technique allowed for improving the electrical conductivity and strength of YSZ–NiO(Ni) cermet (Table 1 and Figure 2a,b).

Significantly more intensive interdiffusion of nickel and oxygen occurred on boundaries of Ni-phase particles during redox treatment of as-sintered anode ceramics at 600 °C in pure hydrogen (mode 5 in Table 1 and Figure 5c). The microstructure image of the obtained cermet in mode 5 exhibits small and large completely reduced Ni-phase particles of gray color. The large ones have signs of thick Ni-fringes of light-gray color formed during the cyclic reduction/oxidation process. This microstructure allowed for a further increase in electrical conductivity of YSZ–NiO(Ni) cermet (Table 1 and Figure 2b).

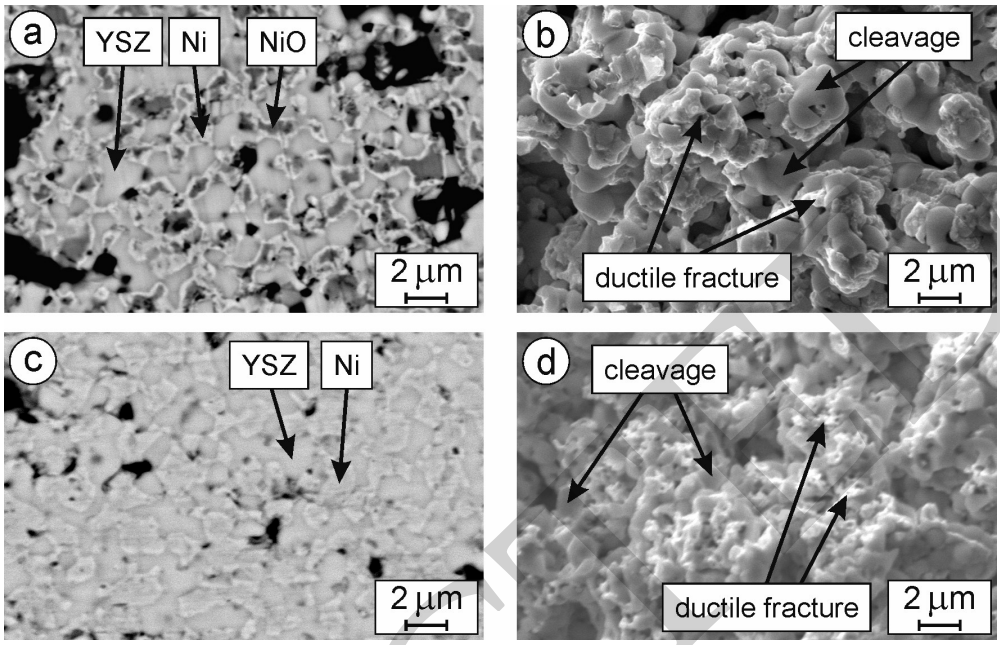

Figure 5. SEM images of (**a**,**c**) microstructure (BSD mode) and (**b**,**d**) fracture surface (SE mode) for treated YSZ–NiO ceramics according to (**a**,**b**) mode 4 and (**c**,**d**) mode 5 (Table 1). Arrows indicate the YSZ, NiO, and Ni phases, as well as cleavage and ductile fractures.

3.2. Evolution of Microstructure at a Temperature of 800 °C

For comparison with the above-mentioned treatment modes at 600 °C, we also studied the behavior of YSZ–NiO ceramics at 800 °C. This temperature allows for shortening the time of both the reduction and oxidation processes. During one-time exposition of the material in Ar–5 vol%H_2 mixture at 800 °C (mode 6 in Table 1), NiO particles were completely reduced within 1 h (Figure 6a). Here, kinetic mechanism [30,31,33–36] was implemented for which there is no limitation in the access of reagents, and a significantly higher reduction intensity occurred as compared to that for mode 2. As a result, nanopores appeared in completely reduced Ni particles. Spectrum S1 (Figure 6a and Table 4) showed two times lower weight percentages of Zr and Y as compared to spectrum S1 in mode 2 (Table 2), whereas the percentage of Ni is significantly higher. Therefore, spectrum S1 in mode 6 corresponds to the YSZ phase with small particles of reduced Ni. Spectrum S2 in mode 6 (Figure 6a and Table 4) showed a slightly higher percentage of Ni, whereas weight percentages of Zr and Y were slightly lower compared to spectrum S1 in this mode. Therefore, spectrum S2 in mode 6 corresponds to the small completely reduced Ni particles which cover the YSZ phase. Complete reduction in the nickel phase resulted in comparatively high electrical conductivity of the cermet, which is commensurate with that for specimens in modes 3, 4, and 5 (Figure 2b).

Table 4. The data of the EDX spectra S1 and S2 marked in Figure 6a for a specimen treated in mode 6.

Chemical Element and X-ray Series	Spectra			
	S1		S2	
	wt%	at%	wt%	at%
O K	11.20	34.86	11.89	36.06
Ni K	54.95	46.61	57.91	47.83
Y L	3.55	1.99	3.14	1.72
Zr L	30.30	16.54	27.06	14.39

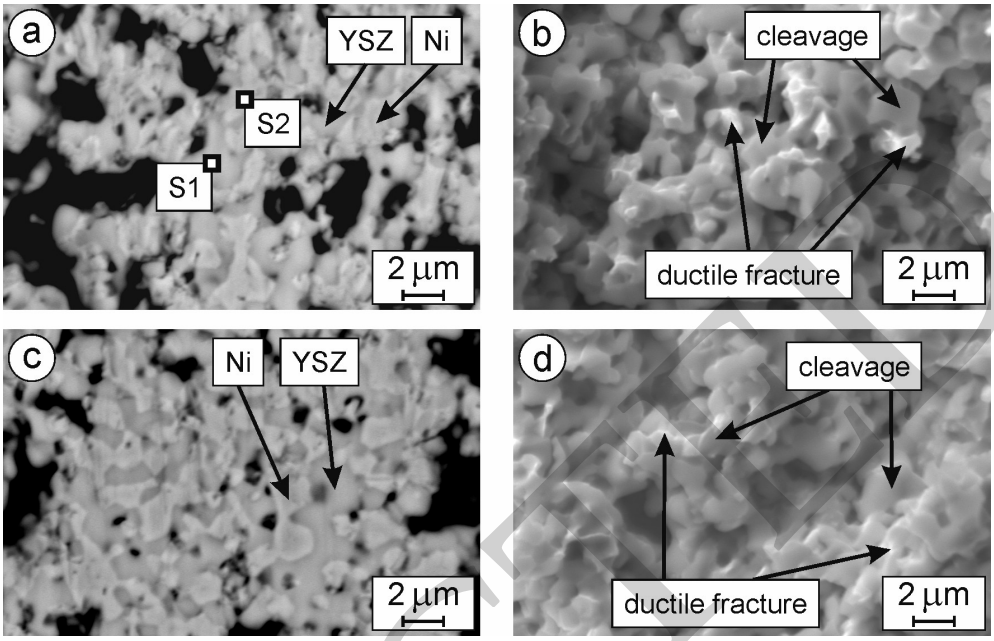

Figure 6. SEM images of (**a**,**c**) microstructure (BSD mode) and (**b**,**d**) fracture surface (SE mode) for treated YSZ–NiO ceramics according to (**a**,**b**) mode 6 and (**c**,**d**) mode 7 (Table 1). Spectra of local EDX analyses S1 and S2 are marked in SEM image (**a**). Arrows indicate the YSZ and Ni phases, as well as cleavage and ductile fractures.

An increase in the exposition time to 2 h (mode 7 in Figure 6c) caused complete reduction in the nickel phase with the same high intensity as in mode 6. However, a slightly lower conductivity of the cermet was achieved as compared to that of specimens in modes 3–6 (Figure 2b). This drop in conductivity is clearly attributed to the redistribution of reduced nickel particles at 800 °C (Figure 6c).

A cermet obtained due to the redox treatment of YSZ–NiO ceramics at 800 °C for 1 h in Ar–5% H_2/air atmosphere (mode 8 in Table 1) exhibited the microstructure patterns of the outer layer (Figure 7a) and the specimen core (Figure 7c) with completely reduced Ni particles. A complex reduction/oxidation process at 800 °C implemented the kinetic mechanism without limitation in the access of reagents [31,32,34–37]. Spectrum S1 (Figure 7a and Table 5) showed high weight percentages of Zr and Y, which are commensurate with those of spectrum S1 in mode 2 (Table 2). Therefore, spectrum S1 in mode 8 corresponds to the YSZ phase. In contrast, spectrum S2 showed a high weight percentage of Ni and a low percentage of oxygen that corresponds to the Ni phase. However, in contrast to the one-time reduced cermets in modes 6 and 7, comparatively lower electrical conductivity of the cermet in mode 8 was achieved (Figure 2b).

Table 5. The data of the EDX spectra S1 and S2 marked in Figure 7a for a specimen treated in mode 8.

Chemical Element and X-ray Series	Spectra			
	S1		S2	
	wt%	at%	wt%	at%
O K	24.26	68.54	3.12	10.64
Ni K	5.92	3.66	95.34	88.44
Y L	7.19	2.86	–	–
Zr L	62.63	24.94	1.54	0.92

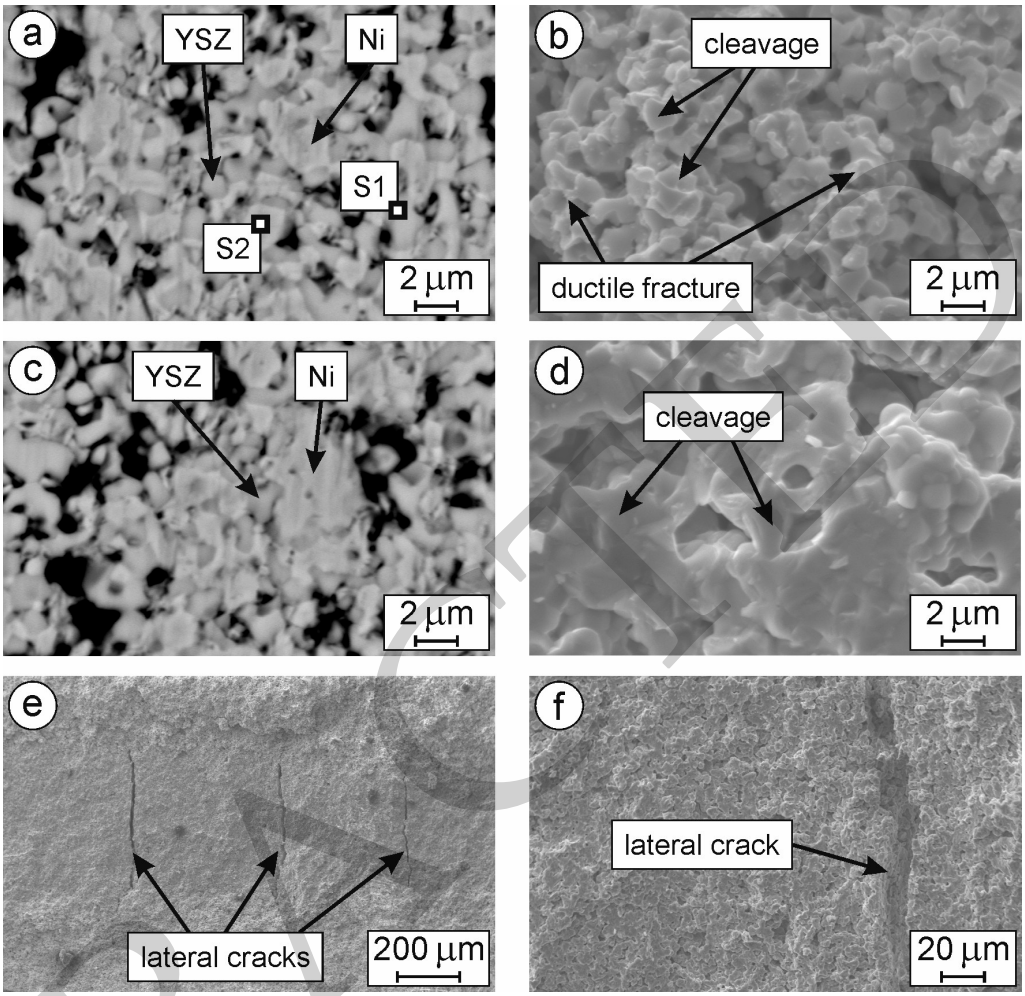

Figure 7. SEM images of (**a**,**c**) microstructure (BSD mode) and (**b**,**d**–**f**) fracture surface (SE mode) for treated YSZ–NiO ceramics according to mode 8 (Table 1) presenting (**a**,**b**) the near-surface layer, (**c**,**d**) the specimen core, and (**e**) low and (**f**) high magnification views of lateral cracks that occurred in the specimen core during the flexure test. Spectra of local EDX analyses S1 and S2 are marked in SEM image (**a**). Arrows indicate the YSZ and Ni phases, as well as cleavage, ductile fractures, and lateral cracks.

4. Discussion

4.1. Microstructure Related Changes in Fracture Micromechanisms

The average size of coherent dispersion areas of nickel phase (parameter *D* in Figure 2c) for the material in mode 2 was estimated as 45 nm, which is about that for mode 1 (as-sintered). Flexural strength of the cermet in this mode was found to be 84 ± 3% of that for as-sintered YSZ–NiO ceramics (Figure 2a). The Bragg's law was applied for evaluating a possible change in 2Θ angle for XRD patterns in corresponding modes:

$$n\lambda = 2d\sin\Theta \quad (5)$$

where n is the diffraction order (positive integer), λ is the wavelength of incident wave, and d is the spacing between the planes in the atomic lattice of the zirconia phase.

No discernible change in 2Θ angle was revealed for the cermet in mode 2 compared to the material in mode 1 (Figure 8). As a result, no significant change in residual stress was found for this material (Figure 2d). Therefore, residual stresses did not contribute significantly to the resulting strength of the cermet. In contrast to the cleavage fracture micromechanism characteristic for the specimens of as-sintered ceramics tested in flexure

(Figure 4b), the mixed fracture micromechanism dominated in the specimens in mode 2. It comprised of cleavage facets of brittle fracture of the zirconia phase and ridges formed due to the plastic stretching of the nickel fringes, i.e., ductile fracture (Figure 4d).

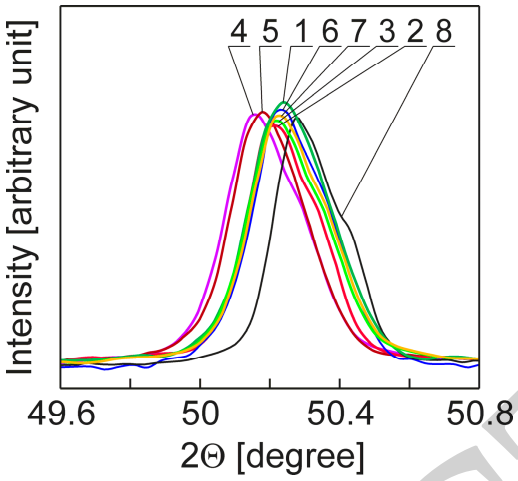

Figure 8. Displacements of the diffraction line (220) of the YSZ phase of material in modes 1–8 (Table 1).

In contrast, the value of parameter *D* for the cermet in mode 3 one-time reduced in pure hydrogen was determined as 41 nm (Figure 2c), which is lower than those for modes 1 and 2. This is an evidence, in addition to the microstructure image (Figure 4c), of a significant change in the nickel-phase structure. As a result of the microstructure transformation, a distinct decrease in flexural strength of the cermet in this mode (48 ± 5.2% of that for the as-sintered YSZ–NiO ceramics) was revealed (Figure 2a). For this cermet, almost no change in 2Θ angle was detected (Figure 8), while a slight change in residual stress was found (Figure 2d). Therefore, residual stresses slightly affected the flexural strength of the cermet, whereas other factors, in particular, the phase-transformation-assisted debonding affected the strength drastically. Specimens of the cermet in mode 3 tested in flexure exhibited predominantly multiple fractures of the plastically stretched nickel particles (ductile fracture) with a small number of cleavage facets of the zirconia phase (Figure 4f), in contrast to the behavior of the material in mode 2.

The value of parameter *D* for the cermet in mode 4 redox-treated at 600 °C for 4 h in Ar–5% H_2/air atmosphere was found as 44 nm (Figure 2c), which is close to that for the material in mode 2. However, a significant shift of the diffraction line (220) of the ZrO_2 phase of this material to the left relative to the corresponding line for the as-sintered material was revealed (Figure 8), which corresponds to an occurrence of significant compressive residual stress (Figure 2d). Diffusion-driven fragmentation and redistribution of nickel-phase particles may be the reason for this as shown by Kharchenko Y. et al. [52]. Compressive residual stresses promote an increase in flexural strength of the material compared to the other reduced cermets (the values of flexural strength and relative strength were found to be 127 ± 4 MPa and 96 ± 2.5%, respectively). In flexure, specimens of the cermet exhibited multiple fractures of the plastically stretched nickel particles that corresponded to higher cohesive strength between the particles of zirconia and nickel phase as compared to the one-time reduced material. The sizes of nickel particles and, consequently, an average cross-sectional area of their fracture (Figure 5b) are significantly smaller than those for the material in mode 2 (Figure 4d). Along with a more pronounced fracture relief exhibiting crack growth along boundaries of agglomerates consisting of fine nickel and zirconia particles, these features are evidences of the comparatively high flexural strength of this cermet.

The cermet in mode 5 redox-treated at 600 °C for 4 h in H_2/air atmosphere exhibited the value of parameter *D* for the cermet 45 nm (Figure 2c), which is close to that for the cermet in mode 4. Quite low relative strength of material in mode 5 (63 ± 3.2%) is attributed

to the loose substructure of external parts of the large Ni-phase particles (former Ni-fringes of light-gray color), which easily fails in flexure. This substructure is manifested in the porous nature of fracture of the nickel-phase particles. However, this behavior is not typical of the small Ni-phase particles redistributed in the material bulk, as they quite densely fail after exhausting the plasticity potential. In addition, quite high compressive residual stress (Figure 2d) occurred in this cermet, which is evidenced by a shift of the diffraction line (220) of the ZrO_2 phase to the left, similarly to that of the material in mode 4 (Figure 8). This stress also contributes positively to a level of flexural strength for this cermet. Therefore, we can see on the fracture surface of the specimen tested in flexure both inter- and trans-granular fractures of zirconia skeleton as well as multiple fractures of the plastically stretched nickel particles (Figure 5d).

Both cermets in modes 6 and 7 one-time reduced at 800 °C in Ar–5% H_2 gas mixture for 1 and 2 h, respectively, showed similar fracture micromechanisms in flexure (Figure 6b,d), namely, inter- and trans-granular fractures of zirconia grains and occasionally ductile fracture of the coagulated nickel particles. The value of parameter *D* for the cermets equal to 46 nm is the same as for the as-sintered ceramics (Figure 2c). No significant shifts of the examined diffraction line (Figure 8) were indicated for these cermets. However, a slightly lower flexural strength of the cermet in mode 7 compared to that in mode 6 is attributed to a higher level of tensile residual stress that occurred in the first (Figure 1d). Nevertheless, it is assumed that one-time reduction at a temperature of 800 °C did not violate the zirconia skeleton integrity.

The cermet in mode 8 redox-treated at 800 °C for 1 h in Ar–5% H_2/air atmosphere exhibited the value of parameter *D* of 58 nm (Figure 2c), which is significantly higher than that for the materials in all other modes. A discernible shift of the examined diffraction line to the right relative to the corresponding line for the as-sintered material and, especially, for materials redox-treated at 600 °C was revealed (Figure 8), which corresponds to an occurrence of significant tensile residual stress (Figure 2d). A discernible microstructure gradient between the near-surface layer (Figure 7a,b) and the specimen core (Figure 7c,d) was detected. Lateral cracks are initiated on these interfaces (i.e., near-surface layer/specimen core and specimen core/near-surface layer according to the specimen positioning) during the flexure test (Figure 7e,f), as a result of a stress gradient. All these features caused a significant decrease in flexural strength of the material (its relative strength is only 33 ± 5%) compared to the cermets in other modes. Dominant fracture micromechanisms were revealed to be cleavage (specimen core, see Figure 7d) and mixed cleavage/intergranular fractures (near-surface layer, see Figure 7b). Therefore, mode 8 (redox treatment at 800 °C) can be indicated as the most inappropriate among the studied modes in terms of both flexural strength and electrical conductivity.

4.2. A Vickers Indentation Test for Evaluating Materials Workability

The Vickers indentation test of the materials in the studied modes can serve as an additional indicator of their workability. We have investigated changes in Vickers microhardness (Figure 9a,b) and fracture toughness measured by the Vickers method (Figure 9c,d) of the anode materials depending on the indentation load. Graphs with magnified ordinate scales (Figure 9b,d) corresponding to the rectangle regions A and B marked in positions (Figure 9a,c), respectively, were used to determine levels of mechanical characteristics corresponding to the indentation load of 9.81 N. This value of the load was the largest one provided by a microhardness tester.

It was found that the microhardness dependences showed a decrease in corresponding values, whereas fracture toughness dependences exhibited a trend to increases in corresponding values. Limits for both these mechanical characteristics (the levels corresponding to the indentation load of 9.81 N) were indicated by horizontal lines. We used these lines (Figure 9b,d) as susceptible mechanical indicators of microstructural changes in the studied materials. It was revealed that the as-sintered material (mode 1) has a significant advantage over other studied materials (modes 2–8) in terms of microhardness and fracture toughness

exhibiting the highest values for both these characteristics (2.2 GPa and 4.2 MPa·m$^{1/2}$, respectively, under the indentation load of 9.81 N). The cermet in mode 2 also had an advantage in both levels of these characteristics (0.82 GPa and 3 MPa·m$^{1/2}$, respectively, under the indentation load of 9.81 N) over cermets in modes 3–8. Materials in modes 4 and 5 are inferior to the cermet in mode 2, still showing comparatively high levels of microhardness and fracture toughness. Finally, materials in modes 3, 6, 7, and 8 exhibited the lowest levels of these characteristics (about 0.65–0.70 GPa and 2.8 MPa·m$^{1/2}$, respectively, under the indentation load of 9.81 N). As an exception, the cermet in mode 8 had the highest microhardness (0.71 GPa under the indentation load of 9.81 N) among the last ones.

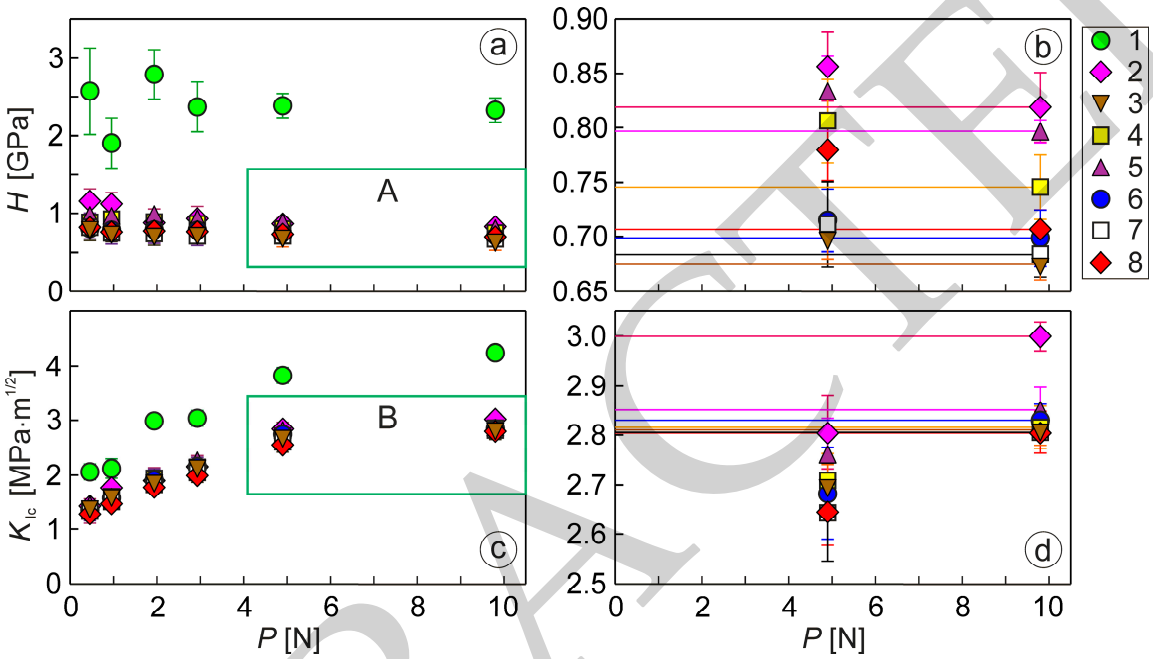

Figure 9. Changes in mechanical characteristics of YSZ–NiO(Ni) anode material in modes 1–8 (Table 1) depending on the indentation load: (**a**,**b**) Vickers microhardness; (**c**,**d**) fracture toughness measured by the Vickers method. Graphs with magnified ordinate scales (**b**,**d**) correspond to the rectangle regions A and B marked in positions (**a**,**c**), respectively. Horizontal lines in positions (**b**,**d**) indicate levels of mechanical characteristics corresponding to the indentation load of 9.81 N.

All these features are related to corresponding microstructures and levels of other parameters (relative strength, size of coherent dispersion areas of nickel phase, and residual stress) for the studied materials. The main advantages of redox-treated material under the best conditions (mode 4) over one-time reduced material under the best conditions (mode 2) in terms of flexural strength and electrical conductivity are as follows: The cermet in mode 4 exhibited values of these characteristics as 127 ± 4 MPa and 7 × 10^5 S/m, respectively, in comparison with 111.1 ± 4.6 MPa and 2.7 × 10^5 S/m for the cermet in mode 2. According to the characteristics of microhardness and fracture toughness, the material in mode 4 is slightly inferior to the material in mode 2: 0.75 GPa and 2.82 MPa·m$^{1/2}$ versus 0.82 GPa and 3 MPa·m$^{1/2}$, respectively.

Therefore, modes 2, 5, and especially 4 can be regarded as promising for preconditioning YSZ–NiO anode ceramics, as materials in these modes exhibited perfect physical, mechanical, and microstructural characteristics. Values of electrical conductivity of Ni–YSZ anodes presented in a review by Faes A. et al. [44] are in the range of 1.2 × 10^5 S/m to 2.4 × 10^5 S/m, which are comparable to those obtained in our study.

Summarizing the obtained results, we can clearly claim that the mode of redox treatment at 600 °C for 4 h in Ar–5% H_2/air atmosphere is promising for preconditioning YSZ–NiO anode ceramics. Significant residual compressive stresses that arose as a result of the treatment contributed to an increase in flexural strength of the material compared to

the other reduced cermets. In addition, a comparatively high level of electrical conductivity was provided for this cermet.

Given the promising mechanical behavior and electrical conductivity of YSZ–NiO anode ceramics that the redox treatment underwent, we will carry out a thorough research in the future on the evolution of submicrostructure in half cycles of reduction and oxidation. This will make it possible to understand the nature of a significant increase in flexural strength of YSZ–NiO(Ni) anode material.

5. Conclusions

1. Redox treatment at 600 °C positively affects flexural strength, microhardness, fracture toughness, and electrical conductivity of YSZ–NiO(Ni) anode cermets.
2. In contrast, this treatment at 800 °C causes the formation of a gradient microstructure. Lateral cracks are initiated on the "near-surface layer/specimen core" interfaces under mechanical loading that causes a significant decrease in flexural strength of the material. The inner layer of the cermet has unsatisfactory electrical conductivity.
3. The mode of redox treatment at 600 °C for 4 h in Ar–5% H_2/air atmosphere can be regarded as promising for preconditioning YSZ–NiO anode ceramics, as materials in this mode exhibited the best physical, mechanical, and microstructural characteristics. Significant residual compressive stresses that arose as a result of the treatment contributed to an increase in flexural strength of the material compared to the other reduced cermets (the values of flexural strength and relative strength were 127 ± 4 MPa and 96 ± 2.5%, respectively), while electrical conductivity was provided at a comparatively high level (7×10^5 S/m). High flexural strength of this cermet was also substantiated in terms of a pronounced fracture relief exhibiting crack growth along boundaries of agglomerates consisting of fine nickel and zirconia particles. This material also has an advantage in terms of microhardness and fracture toughness (0.75 GPa and 2.82 MPa·$m^{1/2}$, respectively, under the indentation load of 9.81 N) over those redox-treated at 800 °C (0.68–0.71 GPa and 2.80–2.81 MPa·$m^{1/2}$, respectively).
4. The above experimental data and performed analyses verify the feasibility of redox technique in appropriate modes for preconditioning Ni-containing SOFC anode materials rather than using a traditional one-time reduction process.

Author Contributions: Conceptualization, B.V., V.K. and Z.D.; methodology, V.K. and B.V.; formal analysis, Z.D. and T.K.; investigation, B.V. and T.K.; writing—original draft preparation, B.V. and V.K.; writing—review and editing, Z.D., V.K. and B.V.; supervision, B.V. and V.K.; funding acquisition, V.K., B.V. and Z.D. All authors have read and agreed to the published version of the manuscript.

Funding: This research was supported by the Ministry of Education and Science of Ukraine under the project number 0122U000952, "Development of a scientific basis for the creation of multifunctional oxide ceramic materials and coatings".

Data Availability Statement: All the supporting and actual data are presented in the manuscript.

Acknowledgments: The authors are thankful to the staff of the Scientific Equipment Collective Use Center "Laboratory of Advanced Technologies, Creation and Physicochemical Analysis of a New Substances and Functional Materials" at Lviv Polytechnic National University (https://lpnu.ua/ckkno (accessed on 20 July 2022)) for their kind help in performing X-ray diffraction studies.

Conflicts of Interest: The authors declare no conflict of interest.

References

1. IPCC. *Climate Change 2014: Mitigation of Climate Change. Contribution of Working Group III to the Fifth Assessment Report of the Intergovernmental Panel on Climate Change*; Edenhofer, O., Pichs-Madruga, R., Sokona, Y., Farahani, E., Kadner, S., Seyboth, K., Adler, A., Baum, I., Brunner, S., Eickemeier, P., et al., Eds.; Cambridge University Press: Cambridge, UK; New York, NY, USA, 2014. Available online: https://www.ipcc.ch/site/assets/uploads/2018/02/ipcc_wg3_ar5_frontmatter.pdf (accessed on 31 January 2023).
2. Golkhatmi, S.Z.; Asghar, M.I.; Lund, P.D. A review on solid oxide fuel cell durability: Latest progress, mechanisms, and study tools. *Renew. Sustain. Energy Rev.* **2022**, *161*, 112339. [CrossRef]

3. Boldrin, P.; Brandon, N.P. Progress and outlook for solid oxide fuel cells for transportation applications. *Nat. Catal.* **2019**, *2*, 571–577. [CrossRef]
4. Jacobson, A.J. Materials for solid oxide fuel cells. *Chem. Mater.* **2010**, *22*, 660–674. [CrossRef]
5. Zamudio-García, J.; Caizán-Juanarena, L.; Porras-Vázquez, J.M.; Losilla, E.R.; Marrero-López, D. A review on recent advances and trends in symmetrical electrodes for solid oxide cells. *J. Power Sources* **2022**, *520*, 230852. [CrossRef]
6. Connor, P.A.; Yue, X.; Savaniu, C.D.; Price, R.; Triantafyllou, G.; Cassidy, M.; Kerherve, G.; Payne, D.J.; Maher, R.C.; Cohen, L.F.; et al. Tailoring SOFC electrode microstructures for improved performance. *Adv. Energy Mater.* **2018**, *8*, 1800120. [CrossRef]
7. Vasyliv, B.D.; Podhurska, V.Y.; Ostash, O.P.; Vira, V.V. Effect of a hydrogen sulfide-containing atmosphere on the physical and mechanical properties of solid oxide fuel cell materials. In *Nanochemistry, Biotechnology, Nanomaterials, and Their Applications*; Fesenko, O., Yatsenko, L., Eds.; Springer International Publishing AG: Cham, Switzerland, 2018; Volume 214, pp. 475–485. [CrossRef]
8. Bertei, A.; Ruiz-Trejo, E.; Kareh, K.; Yufit, V.; Wang, X.; Tariq, F.; Brandon, N.P. The fractal nature of the three-phase boundary: A heuristic approach to the degradation of nanostructured solid oxide fuel cell anodes. *Nano Energy* **2017**, *38*, 526–536. [CrossRef]
9. Romaniv, O.M.; Vasyliv, B.D. Some features of formation of the structural strength of ceramic materials. *Mater. Sci.* **1998**, *34*, 149–161. [CrossRef]
10. Yoshikawa, M.; Yamamoto, T.; Yasumoto, K.; Mugikura, Y. Degradation analysis of SOFC stack performance: Investigation of cathode sulfur poisoning due to contamination in air. *ECS Trans.* **2017**, *78*, 2347–2354. [CrossRef]
11. Jacobs, R.; Mayeshiba, T.; Booske, J.; Morgan, D. Material discovery and design principles for stable, high activity perovskite cathodes for solid oxide fuel cells. *Adv. Energ. Mater.* **2018**, *8*, 1702708. [CrossRef]
12. Bianco, M.; Linder, M.; Larring, Y.; Greco, F.; Van Herle, J. Lifetime issues for solid oxide fuel cell interconnects. In *Solid Oxide Fuel Cell Lifetime and Reliability*; Brandon, N.P., Ruiz-Trejo, E., Boldrin, P., Eds.; Academic Press: Cambridge, MA, USA, 2017; pp. 121–144. [CrossRef]
13. Huang, W.; Zhang, Y.; Lu, J.; Gao, L.; Zhang, F.; Chen, J.; Omran, M.; Chen, G. Effect of sintering time on the microstructure and stability of Al_2O_3–ZrO_2 composite powders under microwave-assisted sintering. *Ceram. Int.* **2023**, *49*, 8993–8999. [CrossRef]
14. Sanchez, I.; Axinte, D.; Liao, Z.; Gavalda-Diaz, O.; Smith, R. The effect of high strain rate impact in Yttria stabilized zirconia. *Mater. Des.* **2023**, *229*, 111908. [CrossRef]
15. Jung, J.-M.; Kim, G.-N.; Koh, Y.-H.; Kim, H.-E. Manufacturing and characterization of dental crowns made of 5-mol% yttria stabilized zirconia by digital light processing. *Materials* **2023**, *16*, 1447. [CrossRef]
16. Mayinger, F.; Buser, R.; Laier, M.; Schönhoff, L.M.; Kelch, M.; Hampe, R.; Stawarczyk, B. Impact of the material and sintering protocol, layer thickness, and thermomechanical aging on the two-body wear and fracture load of 4Y-TZP crowns. *Clin. Oral Investig.* **2022**, *26*, 6617–6628. [CrossRef]
17. Li, Y.; Sun, H.; Song, J.; Zhang, Z.; Lan, H.; Tian, L.; Xie, K. Effect of two-step sintering on the mechanical and electrical properties of 5YSZ and 8YSZ ceramics. *Materials* **2023**, *16*, 2019. [CrossRef] [PubMed]
18. Aziz, A.J.A.; Baharuddin, N.A.; Somalu, M.R.; Muchtar, A. Review of composite cathodes for intermediate-temperature solid oxide fuel cell applications. *Ceram. Int.* **2020**, *46*, 23314–23325. [CrossRef]
19. Li, Q.-L.; Jiang, Y.-Y.; Wei, Y.-R.; Swain, M.V.; Yao, M.-F.; Li, D.-S.; Wei, T.; Jian, Y.-T.; Zhao, K.; Wang, X.-D. The influence of yttria content on the microstructure, phase stability and mechanical properties of dental zirconia. *Ceram. Int.* **2022**, *48*, 5361–5368. [CrossRef]
20. Golkhatmi, S.Z.; Asghar, M.I.; Lund, P.D. Development and characterization of highly stable electrode inks for low-temperature ceramic fuel cells. *J. Power Sources* **2022**, *552*, 232263. [CrossRef]
21. Huang, W.; Qiu, H.; Zhang, Y.; Zhang, F.; Gao, L.; Omran, M.; Chen, G. Microstructure and phase transformation behavior of Al_2O_3–ZrO_2 under microwave sintering. *Ceram. Int.* **2023**, *49*, 4855–4862. [CrossRef]
22. Romaniv, O.M.; Zalite, I.V.; Simin'kovych, V.M.; Tkach, O.N.; Vasyliv, B.D. Effect of the concentration of zirconium dioxide on the fracture resistance of Al_2O_3–ZrO_2 ceramics. *Mater. Sci.* **1996**, *31*, 588–594. [CrossRef]
23. Fan, L.; Zhu, B.; Su, P.C.; He, C. Nanomaterials and technologies for low temperature solid oxide fuel cells: Recent advances, challenges and opportunities. *Nano Energy* **2018**, *45*, 148–176. [CrossRef]
24. Nonaka, K.; Teramae, M.; Pezzotti, G. Evaluation of the effect of high-speed sintering on the properties of 5 mol% yttria stabilized dental zirconia sintered bodies. *Materials* **2022**, *15*, 5685. [CrossRef]
25. Kulyk, V.; Duriagina, Z.; Vasyliv, B.; Vavrukh, V.; Kovbasiuk, T.; Lyutyy, P.; Vira, V. The effect of sintering temperature on the phase composition, microstructure, and mechanical properties of yttria-stabilized zirconia. *Materials* **2022**, *15*, 2707. [CrossRef]
26. Tu, B.; Yin, Y.; Zhang, F.; Su, X.; Lyu, X.; Cheng, M. High performance of direct methane-fuelled solid oxide fuel cell with samarium modified nickel-based anode. *Int. J. Hydrog. Energy* **2020**, *45*, 27587–27596. [CrossRef]
27. Vasyliv, B.; Kulyk, V.; Duriagina, Z.; Mierzwinski, D.; Kovbasiuk, T.; Tepla, T. Estimation of the effect of redox treatment on microstructure and tendency to brittle fracture of anode materials of YSZ–NiO(Ni) system. *East. Eur. J. Enterp. Technol.* **2020**, *6*, 61–71. [CrossRef]
28. Sciazko, A.; Komatsu, Y.; Yokoi, R.; Shimura, T.; Shikazono, N. Effects of mass fraction of $La_{0.9}Sr_{0.1}Cr_{0.5}Mn_{0.5}O_{3-\delta}$ and $Gd_{0.1}Ce_{0.9}O_{2-\delta}$ composite anodes for nickel free solid oxide fuel cells. *J. Eur. Ceram. Soc.* **2022**, *42*, 1556–1567. [CrossRef]

29. He, A.; Gong, J.; Onishi, J.; Shikazono, N. Three-dimensional topology optimization of Ni-YSZ anode for solid oxide fuel cells via multiphase level-set method. *Nano Energy* **2022**, *103*, 107817. [CrossRef]
30. Wood, T.; Ivey, D.G. Chapter 4-The impact of redox cycling on solid oxide fuel cell lifetime. In *Solid Oxide Fuel Cell Lifetime and Reliability*; Brandon, N.P., Ruiz-Trejo, E., Boldrin, P., Eds.; Academic Press: Cambridge, MA, USA, 2017; pp. 51–77. [CrossRef]
31. Tikekar, N.; Armstrong, T.; Virkar, A. Reduction and reoxidation kinetics of nikel-based SOFC anodes. *J. Electrochem. Soc.* **2006**, *153*, A654–A663. [CrossRef]
32. Sarantaridis, D.; Atkinson, A. Redox cycling of Ni-based solid oxide fuel cell anodes: A review. *Fuel Cells* **2007**, *3*, 246–258. [CrossRef]
33. Sun, B.; Rudkin, R.A.; Atkinson, A. Effect of thermal cycling on residual stress and curvature of anode-supported SOFCs. *Fuel Cells* **2009**, *6*, 805–813. [CrossRef]
34. Zhang, Y.; Liu, B.; Tu, B.; Dong, Y.; Cheng, M. Redox cycling of Ni–YSZ anode investigated by TRP technique. *Solid State Ion.* **2005**, *176*, 2193–2199. [CrossRef]
35. Faes, A.; Nakajo, A.; Hessler-Wyser, A.; Dubois, D.; Brisse, A.; Modena, S.; Van Herle, J. RedOx study of anode-supported solid oxide fuel cell. *J. Power Sources* **2009**, *193*, 55–64. [CrossRef]
36. Wood, A.; Waldbillig, D. Preconditioning Treatment to Enhance Redox Tolerance of Solid Oxide Fuel Cells. U.S. Patent 8,029,946 B2, 4 October 2011.
37. Waldbillig, D.; Wood, A.; Ivey, D.G. Electrochemical and microstructural characterization of the redox tolerance of solid oxide fuel cell anodes. *J. Power Sources* **2005**, *145*, 206–215. [CrossRef]
38. Li, J.; Zhu, R.; Yuan, J.; Lu, X.; Zhao, S.; Xu, M.; Huang, J.; Tu, Y.; Jiang, J.; Deng, L.; et al. Phase stability, microstructure and mechanical properties of nanostructured yttria stabilized zirconia coatings subjected to moisture degradation. *Ceram. Int.* **2022**, *48*, 31800–31810. [CrossRef]
39. Mack, J.B.; Pennell, S.M.; Dunand, D.C. Microstructural evolution of lamellar Fe-25Ni foams during steam-hydrogen redox cycling. *Acta Mater.* **2022**, *237*, 118148. [CrossRef]
40. Pennell, S.; Dunand, D. Effects of bridging fibers on the evolution of lamellar architecture during H_2/H_2O redox cycling of Fe-foams. *Acta Mater.* **2023**, *243*, 118543. [CrossRef]
41. Wang, M.; Li, N.; Wang, Z.; Chen, C.; Zhan, Z. Electrochemical performance and redox stability of solid oxide fuel cells supported on dual-layered anodes of Ni–YSZ cermet and Ni–Fe alloy. *Int. J. Hydrog. Energy* **2022**, *47*, 5453–5461. [CrossRef]
42. Chang, H.; Chen, H.; Yang, G.; Shi, J.; Zhou, W.; Bai, J.; Wang, Y.; Li, S.D. Enhanced coking resistance of Ni cermet anodes for solid oxide fuel cells based on methane on-cell reforming by a redox-stable double-perovskite $Sr_2MoFeO_{6-\delta}$. *Int. J. Energy Res.* **2018**, *43*, 2527–2537. [CrossRef]
43. Lv, H.; Huang, Z.; Zhang, G.; Chen, T.; Wang, S. A new design of metal supported micro-tubular solid oxide fuel cell with sandwich structure. *Int. J. Hydrog. Energy* **2022**, *47*, 33420–33428. [CrossRef]
44. Faes, A.; Hessler-Wyser, A.; Zryd, A.; Van Herle, J. A review of RedOx cycling of solid oxide fuel cell anode. *Membranes* **2012**, *2*, 585–664. [CrossRef]
45. Ettler, M.; Timmermann, H.; Malzbender, J.; Weber, A.; Menzler, N.H. Durability of Ni anodes during reoxidation cycles. *J. Power Sources* **2010**, *195*, 5452–5467. [CrossRef]
46. Peraldi, R.; Monceau, D.; Pieraggi, B. Correlations between growth kinetics and microstructure for scales formed by high-temperature oxidation of pure nickel. I. Morphologies and microstructures. *Oxid. Met.* **2002**, *58*, 249–273. [CrossRef]
47. Mori, M.; Yamamoto, T.; Itoh, H.; Inaba, H.; Tagawa, H. Thermal expansion of nickel-zirconia anodes in solid oxide fuel cells during fabrication and operation. *J. Electrochem. Soc.* **1998**, *145*, 1374–1381. [CrossRef]
48. Pihlatie, M.; Ramos, T.; Kaiser, A. Testing and improving the redox stability of Ni-based solid oxide fuel cells. *J. Power Sources* **2009**, *193*, 322–330. [CrossRef]
49. Lang, M.; Raab, S.; Lemcke, M.S.; Bohn, C.; Pysik, M. Long-term behavior of a solid oxide electrolyzer (SOEC) stack. *Fuel Cells* **2020**, *20*, 690–700. [CrossRef]
50. Ostash, O.P.; Vasyliv, B.D.; Podhurs'ka, V.Y.; Vasyl'ev, O.D.; Brodnikovs'kyi, E.M.; Ushkalov, L.M. Optimization of the properties of 10Sc1CeSZ–NiO composite by the redox treatment. *Mater. Sci.* **2011**, *46*, 653–658. [CrossRef]
51. Vasyliv, B.D.; Podhurs'ka, V.Y.; Ostash, O.P.; Vasyl'ev, O.D.; Brodnikovs'kyi, E.M. Influence of reducing and oxidizing media on the physicomechanical properties of ScCeSZ–NiO and YSZ–NiO ceramics. *Mater. Sci.* **2013**, *49*, 135–144. [CrossRef]
52. Kharchenko, Y.; Blikharskyy, Z.; Vira, V.; Vasyliv, B.D.; Podhurska, V.Y.; Kalynovskyy, A.; Korendiy, V. Nanostructural changes in a Ni/NiO cermet during high-temperature reduction and reoxidation. In *Nanomaterials and Nanocomposites, Nanostructure Surfaces, and Their Applications*; Fesenko, O., Yatsenko, L., Eds.; Springer International Publishing AG: Cham, Switzerland, 2021; Volume 246, pp. 219–229. [CrossRef]
53. Gere, J.M.; Timoshenko, S.P. *Mechanics of Materials*, 4th ed.; PWS Publishing Company: Boston, MA, USA, 1997; p. 912.
54. *ASTM E384-11*; Standard Test Method for Knoop and Vickers Hardness of Materials. ASTM International: West Conshohocken, PA, USA, 2011. [CrossRef]
55. *ASTM C1327-03*; Standard Test Method for Vickers Indentation Hardness of Advanced Ceramics. ASTM International: West Conshohocken, PA, USA, 2003. [CrossRef]
56. Anstis, G.R.; Chantikul, P.; Lawn, B.R.; Marshall, D.B. A critical evaluation of indentation techniques for measuring fracture toughness: I, Direct crack measurements. *J. Am. Ceram. Soc.* **1981**, *64*, 533–538. [CrossRef]

57. WinCSD. A Crystal Structure Determination and Crystallographic Calculation Software. Available online: https://www.wincsd.eu/ (accessed on 20 March 2022).
58. *ASTM F43-99*; Test Methods for Resistivity of Semiconductor Materials. ASTM International: SEMI, CA, USA, 2005. Available online: https://www.scribd.com/document/228100659/astm-F43-99 (accessed on 16 August 2022).